INSTITUTE OF PHYSICS PUBLISHING NANOTECHNOLOGY

Nanotechnology **17** (2006) 3428–3435 doi:10.1088/0957-4484/17/14/014

Silver electrodeposition on nanostructured gold: from nanodots to nanoripples

P C dos Santos Claro[1], M Fonticelli[1], G Benítez[1], O Azzaroni[1], P L Schilardi[1], N B Luque[2], E Leiva[2] and R C Salvarezza[1,3]

[1] Instituto de Investigaciones Fisicoquímicas Teóricas y Aplicadas (INIFTA), Facultad de Ciencias Exactas, Universidad Nacional de La Plata—CONICET, Sucursal 4 Casilla de Correo 16 (1900) La Plata, Argentina

[2] Unidad de Matemática y Física, Facultad de Ciencias Químicas Universidad Nacional de Córdoba, Argentina

E-mail: robsalva@inifta.unlp.edu.ar

Received 18 April 2006, in final form 23 May 2006
Published 20 June 2006
Online at stacks.iop.org/Nano/17/3428

Abstract

Silver nanodots and nanoripples have been grown on nanocavity-patterned polycrystalline Au templates by controlled electrodeposition. The initial step is the growth of a first continuous Ag monolayer followed by preferential deposition at nanocavities. The Ag-coated nanocavities act as preferred sites for instantaneous nucleation and growth of the three-dimensional metallic centres. By controlling the amount of deposited Ag, dots of ∼50 nm average size and ∼4 nm average height can be grown with spatial and size distributions dictated by the template. The dots are in a metastable state. Further Ag deposition drives the dot surface structure to nanoripple formation. Results show that electrodeposition on nanopatterned electrodes can be used to prepare a high density of nanostructures with a narrow size distribution and spatial order.

1. Introduction

The preparation of metal and semiconductor nanostructures with defined size and spatial order on metal or semiconductor surfaces is a key point in many fields of nanotechnology [1]. In particular, the preparation of dots and ripples in different materials has attracted considerable attention. Ion sputtering-induced ripple structures have been of particular interest for the fabrication of nanoscale textured materials via self-organization processes or as templates for the preparation of nanowires, nanorods and nanodots [2]. Ripples have been produced on Cu(110) [3], Si [4] and SiO_2 [5] by keV ion bombardment. Metallic ripples have been used as platforms to build anisotropic magnetic nanostructures by deposition of ultrathin layers of transition metals [6]. It has been reported that if the ion beam hits the target straight on instead of at an angle, arrays of nanodots with short-range order instead of ripples can be formed [7].

Semiconductor quantum dots have been also produced by molecular beam epitaxy and metal organic chemical vapour deposition on a foreign substrate following the Stranski–Krastanov (S–K) growth mode [8]. In this case the strain resulting from lattice mismatch between the deposited material and the substrate is the driving force for three-dimensional (3D) growth on the first deposited layer. Limitations of this approach for obtaining spatial order result from the preferential nucleation at substrate defects such as step edges. On the other hand, crystals nucleated on terraces usually exhibit a broad size distribution due to the progressive nucleation and growth of crystals. Therefore, deposits that are rather heterogeneous in shape and size are produced. In order to solve this problem patterned substrates can be used. The patterned areas can act as preferred sites for nucleation. In this way a controlled arrangement of self-organized Ge islands on patterned Si(001) substrates has been produced [9]. In other cases, the patterns are introduced by a 'one by one' writing by using atomic force microscopy (AFM) or scanning tunnelling microscopy (STM) tips. Following this approach 20 nm quantum dots have been prepared by local oxidation of silicon by a AFM tip, followed by oxide removal by etching, and finally by the self-assembly of semiconductor quantum dots by S–K growth in a molecular beam epitaxy chamber [10].

[3] Author to whom any correspondence should be addressed.

Metal electrodeposition is a well known technique involving relatively low cost equipment, and it is currently used in many technological applications [11]. Electrochemical fabrication of large arrays of metal nanoclusters by using a STM tip has been described [12]. However, large scale patterning of the substrate by 'one by one' fabrication is rather difficult and time consuming. Electrodeposition on patterned templates is particularly attractive for building metallic, oxide and semiconductor nano/microstructures [13] because extremely small amounts of material can be deposited in a controlled way by changing the applied potential (or current). Besides, different crystal sizes and shapes can be obtained by changing the kinetic control of the electrochemical reactions [14]. Metallic deposits can be easily transformed in oxide or sulfide-coated nanostructures by simple electrochemical or chemical reactions. Semiconductor nanodots on patterned metal films are important because surface plasmons of the nanostructured surface are expected to improve the photonic properties of the semiconductor nanocrystals [15]. In practice, a metallic film with nanometre-scale surface-roughness features can be used to support surface plasmons and to provide a grating to scatter light into the far field. Like the near-field coupling into the plasmon modes, scattering off this grating can be much faster than radiative emission in nanocrystals [16]. More recently, the formation of a high density of Ag nanoparticles and a novel method to precisely control the spacing between nanoparticles by temperature was reported for tunable surface enhanced Raman scattering substrates. The high-density nanoparticle thin film was accomplished by self-assembly through the Langmuir–Blodgett method [16].

In contrast to metal electrodeposition on well defined substrates [17], our knowledge of this process on nanopatterned electrodes (50 nm range) is rather limited. Important questions that should be addressed in relation to electrodeposition on nanostructured electrodes are: (1) Do the template nanostructures act as preferred sites for nucleation? (2) Is it possible to induce instantaneous nucleation on the template? (3) Can the size of the crystal be controlled in the nanoscale range of the template pattern by the applied potential? (4) How stable are the electrodeposited nanostructures? These questions are important because they are related to the spatial order, size, narrow size distribution and stability of the nanostructures.

In this work we have used electrodeposition to grow Ag nanodots with a surface density of 10^{10}–10^{11} cm^{-2} and nanoripples on Au templates supported on Scotch tape. The initial step is the growth of a first continuous Ag monolayer. When more Ag is electrodeposited the Ag-coated nanocavities act as preferred sites for instantaneous nucleation and growth of the 3D metallic centres. By controlling the amount of deposited Ag, nanodots of ∼50 nm average size and ∼4 nm average height can be grown with a spatial distribution dictated by the template. A simple model indicates that the dots are in a metastable state so that further Ag deposition drives the system to a rippled structure. Electrodeposition on nanopatterned templates can be an attractive route to prepare a high density of nanostructures with a narrow size distribution and spatial ordering in a simple and inexpensive way.

2. Experimental details

2.1. Sample characterization

The surface structure of the deposited nanostructures and templates was determined by atomic force microscopy (AFM) using a Nanoscope IIIa (Digital Instruments, Santa Barbara, CA) operating in the contact mode. AFM imaging was done using Si_3N_4 tips.

The surface chemical composition was analysed by Auger electron spectroscopy (AES) by using a single pass cylindrical mirror analyser (CMA; Physical Electronics). The Auger spectra were measured with the electron gun operated at 3 keV and 10 mA cm^{-2}. The Auger transition is described using the spectroscopic notation for the energy levels involved. Typically two to four different samples and four or five points within a sample were investigated for each condition.

2.2. Template preparation

A silicon master with a surface array of short-range ordered nanodots (∼40–50 nm in size, height 6 nm, dot density ∼10^{11} cm^{-2}) prepared as described in [18] was used to produce metallic templates. The complete procedure for building the templates was described in [19]. Briefly, the SiO_2 surface was chemically modified by immersion in octadecyltrichlorosilane (OTS)-containing hexane solution for 1 h forming a self-assembled silane monolayer [19]. Afterwards, 200 nm thick Au films were deposited by thermal physical vapour deposition (PVD) on the OTS-covered silicon. The deposited polycrystalline metal films were mechanically detached from the OTS-covered master by using Scotch tape due to the excellent anti-adherent properties of the silane monolayers [19]. The inner interface of the metal films (that in contact with the OTS-covered silicon master) after the detachment process is shown in figure 1(a).

The AFM images show an array of nanocavities that have been moulded by the silicon master. The corresponding cross-sections and power spectral density (PSD) show cavities of 3–4 nm in average depth and 42 nm in average size, respectively (figure 1(a)). The root mean square roughness (rms roughness) measured over 1 × 1 μm^2 AFM images is 1.3–1.9 nm. The hump in the PSD (figure 1(b), grey arrow) indicates the size of the small Au grains (15 nm in size) that form the structure of the PVD template. The surface coverage by nanocavities is about half of the total surface.

2.3. Nanostructure preparation

Ag electrodeposition was performed in a conventional three-electrode electrochemical cell, using the Scotch tape supported Au template (figure 1(a)) as the working electrode, a large platinum sheet as the counterelectrode, and a Ag plate as reference electrode. The electrolyte solution was aqueous 1×10^{-3} M $AgNO_3$ + 0.5 M $HClO_4$ at a temperature of $T = 298$ K. Applied potentials to the working electrode in the text are referred to the Ag^+/Ag reversible potential in the electrolyte solution. The electrolyte was degassed with purified nitrogen for 2 h before the electrochemical runs. Ag electrodeposition was performed by applying a linear potential sweep from 0.5 V to the deposition potential E_d. Afterwards,

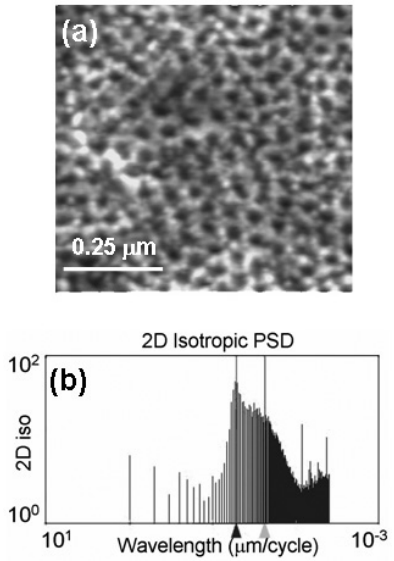

Figure 1. (a) AFM image ($0.75 \times 0.75\ \mu m^2$) of the Scotch tape supported polycrystalline Au template used as substrate for Ag electrodeposition. (b) Power spectral density corresponding to the AFM image after high-pass filtering. The black arrow indicates the average size of the cavities (42 nm) while the grey arrow indicates the size of small grains (15 nm) that form the Au deposit.

the Ag-covered Au template was removed from the solution, rinsed with MilliQ water and dried under nitrogen before the AFM and AES characterization.

3. Results and discussion

3.1. Experimental results

The typical current density (j)/potential (E) profile for Ag electrodeposition on the Au template in the underpotential deposition (upd) range (figure 2(a)) exhibits two broad peaks CI and CII at 0.4 and 0.22 V, respectively, corresponding to the electrodeposition of a first Ag monolayer on Au [20]. A more defined peak (CIII) is observed also at 0.0 V corresponding to a second Ag monolayer.

On the other hand, peaks AIII, AII and AI are related to the stripping of the electrodeposited Ag at peaks CIII, CII and CI, respectively. At $E < 0$ the overpotential deposition (opd) of bulk Ag takes place at current peak CIV, whereas the bulk Ag deposit is stripped from the Au template at peak AIV (figure 2(b)) [21].

The Ag upd and opd voltammograms for the nanopatterned Au substrate (figure 1(a)) closely resemble those observed for polycrystalline Au substrates [21]. The shape of the cathodic peak CIV and the limiting current observed at more negative potential values indicate that Ag bulk electrodeposition is under diffusion control of Ag^+ from the solution side [21].

We have prepared different samples by applying a potential sweep to the Au template from 0.5 V to E_d values slightly more negative than the reversible potential (E_r) for bulk Ag electrodeposition. Afterwards the samples were removed from the cell, carefully rinsed with nitrogen-saturated MilliQ water, dried under nitrogen, and finally placed in a high vacuum chamber for AES analysis.

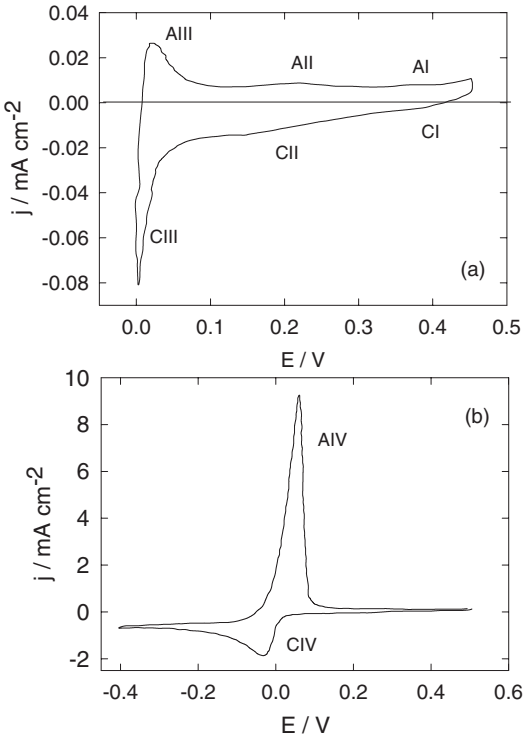

Figure 2. Typical j versus E profiles recorded at 0.01 V s^{-1} for a Scotch tape supported Au template in $AgNO_3$ 1×10^{-3} M + $HClO_4$ 0.5 M covering (a) the Ag upd range and (b) the Ag opd region.

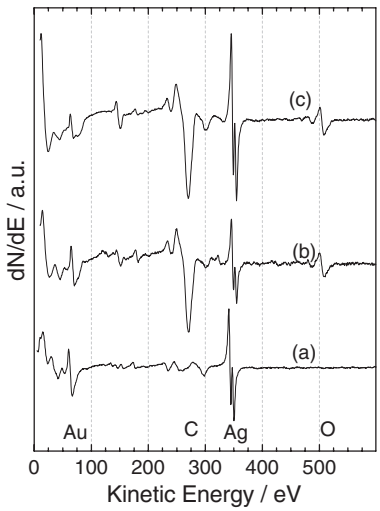

Figure 3. AES spectra of Au electrodes after Ag electrodeposition at different E_d values: (a) plain Au electrode $E_d = -0.01$ V, (b) Scotch tape supported Au template, $E_d = -0.01$ V, (c) Scotch tape supported Au template, $E_d = -0.04$ V.

The AES spectra corresponding to a plain Au electrode and a Scotch tape supported Au template both polarized at $E_d = -0.01$ V are shown in figures 3(a) and (b), respectively. In both cases the Ag and Au signals are clearly visible. From the Ag/Au signal ratio we concluded that ~2 Ag monolayers (ML) have been deposited [22]. Integration of the current density from 0.5 to −0.01 V leads to a charge density $Q \sim 0.4$ mC cm^{-2} (a figure equivalent to 2 ML for a polycrystalline

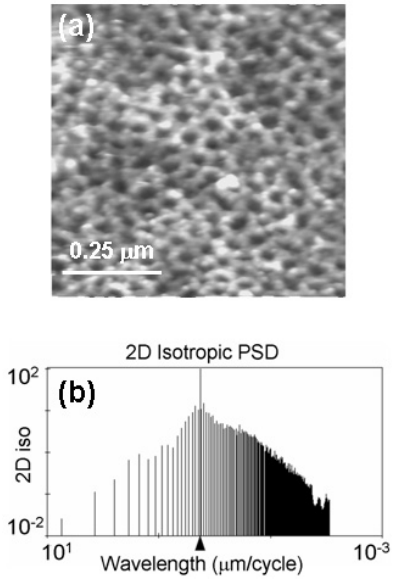

Figure 4. (a) AFM image ($0.75 \times 0.75\ \mu m^2$) of 2 ML Ag-covered gold template after polarization up to $E_d = -0.01$ V in the working solution. (b) Power spectral density corresponding to the AFM image after high-pass filtering. The arrow indicates the average size of the Ag-coated cavities (43 nm).

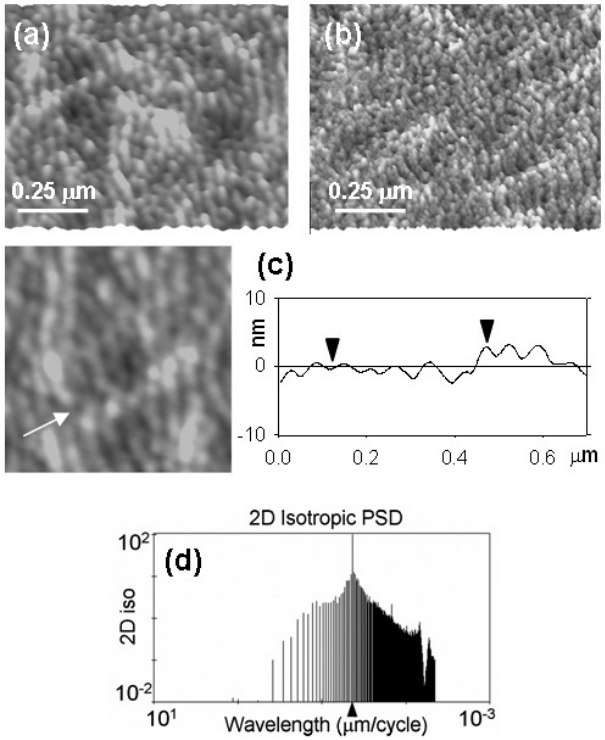

Figure 5. ((a), (b)) 3D AFM images ($1 \times 1\ \mu m^2$, pitch: 53°) of Ag-covered gold after polarization up to $E_d = -0.01$ V in the working solution. Regions with the predominance of dots (a) and cavities (b) are observed. (c) Left: $0.65 \times 0.65\ \mu m^2$ AFM image. The arrow indicates the direction used for the cross-section analysis shown at the right. Cavities (left arrow) and nanodots (right arrow) are indicated. (d) Power spectral density corresponding to a typical $0.75 \times 0.75\ \mu m^2$ AFM image of dots after high-pass filtering. The arrow indicates the average dot size (43 nm).

Au electrode) in good agreement with the AES data. As E_d is shifted in the negative direction ($E_d = -0.04$ V) the amount of Ag increases (figure 3(c)), as concluded from the increase in the Ag/Au intensity ratio.

The C signal, also visible in the template sample, originates from the Scotch tape due to the presence of some pinholes in the 200 nm thick PVD Au film. The small oxygen signal indicates that the electrodeposited nanostructures remain mainly as metallic Ag.

AFM images after deposition of 1 ML ($E_d = 0.0$ V) show no differences from those obtained for the uncovered Au template (figure 1(a)). Cavity size, cavity depth and rms roughness (a measure of the surface amplitude) remain unchanged, indicating that the first ML forms a continuous layer on the patterned substrate. When 2 ML ($E_d = -0.01$ V) are deposited, the cavity size also remains unchanged (figure 4(a)) with respect to the uncovered Au template. However, we noticed that the cavity depth and the rms roughness are reduced to ~2 nm and 0.7–0.6 nm, respectively.

This means that the second silver monolayer has been preferentially deposited at the nanocavities. This fact seems to be mediated by the template because it is well known that two epitaxial Ag layers are deposited at E_d values close to E_r on smooth Au surfaces [20]. Note that this conclusion is based on the decrease in the cavity depth and rms roughness values with respect to the uncovered substrate. Note also that taking into account the effective attenuation length of the Au NVV and Ag MNN electrons, the AES spectrum of this deposit (figure 3(b)) can be explained either by a continuous two monolayer film or by patches of Ag with a height of 3 ML over a continuous monolayer of silver on gold.

When the deposited charge density is increased to $Q \sim 0.5$–0.6 mC cm^{-2}, ($E_d = -0.02$ V, 2.5–3 ML) the AFM images show in some regions nanometre-sized Ag dots nucleated at the nanocavities of the Au template (figure 5(a)). This is clearly seen in figure 5(a), where dots and some unfilled nanocavities coexist. However, many electrode regions show only some dots and a net predominance of cavities that are not completely filled as shown in figure 5(b). The uncovered cavities are 2 nm in depth (figure 5(c), cross-section) like those formed for 2 ML (figure 4). The cross-section analysis also shows that the dots emerge from the cavity edges. As the nanocavities are 3–4 nm in depth the total dot height is 4–5 nm. In this case the rms roughness increases to 1 nm, approaching the value observed for the Au template. The average size of the dots estimated from the PSD analysis is ~50 nm (figure 5(d)). The narrow size distribution indicates that instantaneous nucleation of Ag nanodots takes place on some regions of the patterned Au template. Note that there are also extended areas where no significant dot nucleation takes place (figure 5(b)).

The fact that 2 ML of the ~3 ML (the first layer is continuous) are concentrated in the cavities and the coexistence of large areas where dots are absent explains why dots emerge from the cavity edges. In fact, considering that the amount of Ag corresponding to the second and third monolayers is concentrated in cavities and that the surface coverage by the cavities is half of the total area we have at these sites the first ML plus 4 ML. However, if one considers that only a third

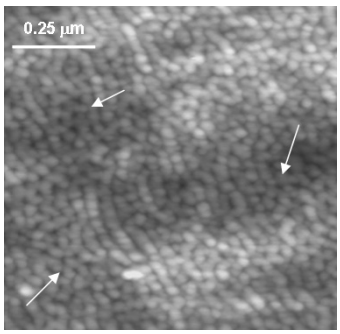

Figure 6. 1.25 × 1.25 μm^2 AFM image after stripping the Ag dots shown in figures 5(a) and (b) in 0.5 M $HClO_4$ by a linear potential sweep up to 1.2 V. The arrows indicate regions where the nanocavities are recovered.

to a quarter of the total cavities have nucleated dots we have at the cavities the first layer plus 12–16 ML, i.e. 3.3–4.25 nm in height. This estimation explains why the dots can emerge from cavities 3–4 nm in depth. Note that this explanation requires that the second ML was preferentially deposited in cavities, a fact supported by the decrease in the rms roughness values of the electrodes measured from the AFM images. This fact contrasts with previous '*in situ*' STM data for Ag electrodeposition on smooth Au(111) [23] that have shown that 3D growth only initiates after completion of a uniform second adlayer. A discussion on the influence of the nanopatterned substrate to induce cavity filling is presented at the end of the paper.

Most of the Ag dots can be eliminated from the template by a linear potential scan from E_d to 1.2 V in a 0.5 M $HClO_4$ solution (figure 6). In these regions the Au template structure is recovered with rms roughness ∼1.3 and depth cavity ∼3–4 nm.

When electrodeposition is made up to $E_d = -0.04$ V ($Q \sim 1$ mC cm^{-2}) the AFM images (figure 7) show that dots tend to grow following preferred directions leading to a rippled structure. We have imaged two different structures with wavelengths of 82 nm (figures 7(a) and (b)) and 62 nm (figures 7(d) and (e)) defined across the ripples. The former corresponds to an open structure formed by alternating rows of dots and cavities. The dots have an average size of 50 nm. The second rippled structure corresponds to a more compact array of dots of average size 60 nm that is formed by the lateral growth of the smaller dots.

It should be noted that we failed to observe dots and ripples when similar amounts of Ag were deposited on smooth Au substrates. In this case isolated flat Ag islands nucleated at step edges are present on the terraces (figure 8).

On the other hand, the cross-section analysis of the rippled structure shown in figures 7(d) and (e) indicates that the height difference along the ripples is only ∼1 nm while this difference between adjacent ripples is ∼4 nm (figure 7(f)). This means that the 3D growth takes place mainly in the ripple direction, and no significant deposition occurs between them. Accordingly, the rms roughness measured over 1 × 1 μm^2 AFM images increases to 3 nm.

When the potential sweep reaches $E_d = -0.06$ V the Au template is completely covered by small elongated crystals

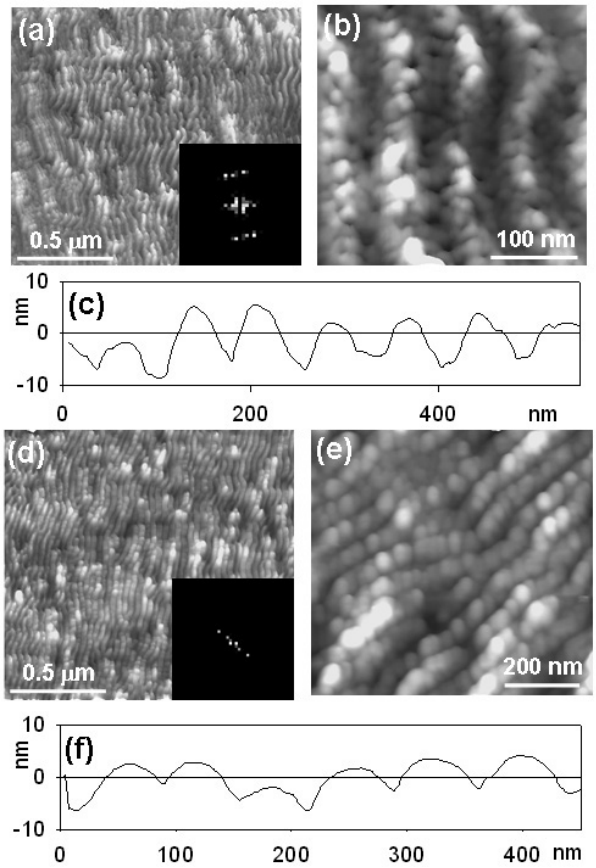

Figure 7. AFM images of rippled structures grown on the Au template after polarization up to $E_d = -0.04$ V in the working solution. (a) 3D AFM image (3 × 3 μm^2, pitch: 63°) showing Ag ripples with 82 nm wavelength. Inset: fast Fourier transformation (FFT) of 2D image corresponding to (b). (b) AFM image (0.31 × 0.31 μm^2) showing a detail of the rippled structure shown in (a). Note the alternating rows of cavities and dots. (c) Cross-section analysis of (b). (d) 3D AFM image (3 × 3 μm^2, pitch: 63°) showing Ag ripples with a wavelength of 62 nm. Inset: FFT of 2D image corresponding to (e). (e) AFM image (0.75 × 0.75 μm^2) showing a detail of the Ag nanodots forming the rippled structure shown in (d). (f) Cross-section analysis of (e).

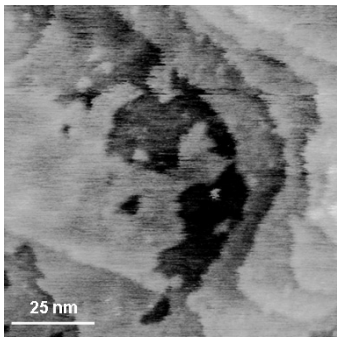

Figure 8. AFM (100 × 100 nm^2) image showing flat islands after ∼1 mC cm^{-2} of electrodeposited Ag on smooth Au.

(60 nm long, 30 nm wide), although a few large crystals (200–500 nm in size) can also be observed (figure 9). No clear evidence of the template was found under this experimental

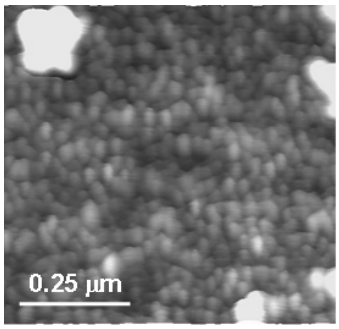

Figure 9. AFM image ($0.75 \times 0.75\ \mu m^2$) of Ag crystals grown on the Au template after polarization up to $E_d = -0.06$ V in the working solution.

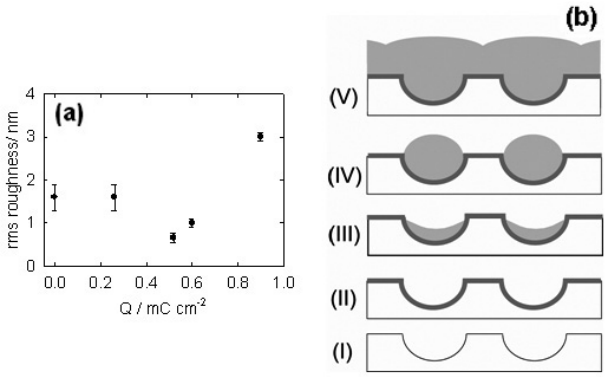

Figure 10. (a) Rms roughness versus Q plot. (b) Scheme showing different stages of Ag templated electrodeposition: (I) Au template, (II) deposition of a continuous ML of Ag, (III) preferential Ag deposition at cavities, (IV) dot formation at nanocavities, (V) preferential growth in some direction leading to ripples.

condition. This means that when the overpotential is large the nucleation rate increases and a large number of smaller crystals are formed at random on the whole surface of the template. However, as the growth process is under diffusion control of Ag^+ from the solution side some instabilities are triggered leading to the formation of large irregular crystals [21].

Our results are summarized in figure 10(a). We have used the rms roughness as a statistical parameter to follow the morphological changes in the system, and Q as a measure of the amount of deposited material. The rms roughness versus Q plot shows, initially, a minimum reflecting the cavity filling, and then a marked increase related to the growth of Ag dots outside the cavities forming ripples. This process is schematically shown in figure 10(b).

It should also be noted that the existence of uniaxial elements that perturb the quasihexagonal arrangement of the template will also contribute to dot coalescence in one direction and then to ripple formation. These elements are present in the Si master prepared by ion bombardment as the balance of dot/ripples in those samples strongly depends on the incident angle [7]. These elements are transferred to the Au template during the moulding procedure explaining the preferred coalescence in one direction.

3.2. Modelling nanostructure stability

A first discussion concerns the early filling of the cavities with respect to the rest of the surface. This is expected on the basis of the chemical bond. The cavities offer sites with a higher coordination, where adatoms may interact more strongly with the surface. This has been confirmed by computer simulations for Cu deposition in Au nanocavities [24] and has been predicted recently for Ag deposition in Au(111) nanocavities [25]. The later simulations predict, in fact, decoration of the bottom of a Au nanocavity by two Ag monolayers previous to its filling. An analysis performed in terms of a continuum model also yields the same qualitative prediction. The chemical potential μ of the adatoms can be written in terms of the geometrical properties of the surface as [26]:

$$\mu = \mu_0 - \tilde{\sigma}\left(\frac{\partial^2 z}{\partial x^2} + \frac{\partial^2 z}{\partial y^2}\right) \tag{1}$$

where μ_0 is the chemical potential of the adatoms on a flat surface, $\tilde{\sigma}$ is the surface stiffness, and the coordinates (x, y, z) denote a point on the surface, with the z coordinate measured perpendicular to it. From this equation, it is clear that a concave surface will lower the chemical potential of the adatoms with respect to those on a flat surface, promoting its filling to minimize the free energy of the system. On the other hand, convex surfaces will be harder to fill than flat ones, resulting in a concomitant overpotential. Thus, the previous argument allows us to understand the processes depicted in the sequences (I)–(III) of figure 10(b).

To analyse the transition from the dots to the ripple regime, we ignore curvature effects in the following simplified discussion and consider the relative stability of dots and ripples, excluding *a priori* other possible structures. A more complete study will be undertaken by means of computer simulations.

For the sake of simplicity we shall assume in all the following discussion that all the atoms located at the border of a given structure have a unique energy. Thus, assuming that the atoms at the border have a higher energy than those within the structure, the most stable figure should be that exhibiting the lowest perimeter for a given surface, that is, a circle. While this is true for an isolated structure, this statement is no longer valid when periodic boundary conditions are applied.

We illustrate both situations in figure 11. While figure 11(a) shows a circle inscribed in a square of side d, figure 10(b) shows a stripe crossing the system.

In the case of the circle, the area S and the perimeter l_{cir} of the circle of radius r are given by:

$$S = \pi r^2 \tag{2}$$

$$l_{cir} = 2\pi r \tag{3}$$

and the surface to perimeter ratio is $\frac{S}{l_{cir}} = \frac{r}{2} = \frac{S^{1/2}}{2\pi^{1/2}}$, where the last equality was written in terms of the area.

Let us now consider a stripe of the same area as the circle. In this case the area and the perimeter are given by:

$$S = d\,h \tag{4}$$

$$l_{str} = 2d \tag{5}$$

where h is the width of the stripe, as illustrated above in figure 10(b), and we have assumed that the stripes cross all

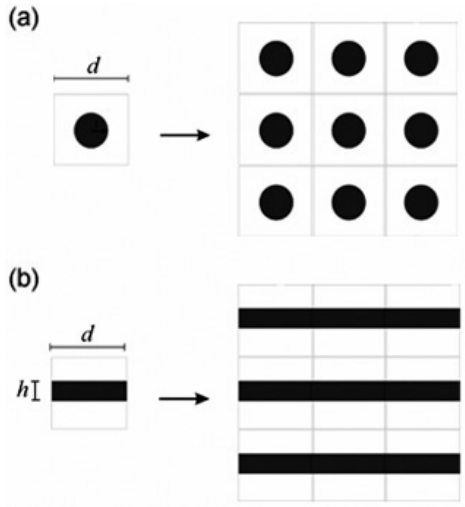

Figure 11. (a) Circular cluster in a square. Its periodical repetition is shown on the right. (b) Rectangular segment in a square. Its periodical repetition leads to stripes.

over the infinite system. In the case of the stripe, the area to perimeter ratio is given by:

$$\frac{S}{l_{\mathrm{str}}} = \frac{h}{2} = \frac{S}{2d}. \tag{6}$$

If we consider the area to perimeter ratio (for the same area S) as a criterion for stability, in the same way, we can consider the ratio γ of the corresponding quantities for the circle and the stripe:

$$\gamma = \frac{\frac{S}{l_{\mathrm{cir}}}}{\frac{S}{l_{\mathrm{str}}}} = \frac{\frac{S^{1/2}}{2\pi^{1/2}}}{\frac{S}{2d}} = \frac{d}{\pi^{1/2} S^{1/2}}. \tag{7}$$

If $\gamma > 1$, the circle will be more stable than the stripe, and the reverse will be true for $\gamma < 1$. In other words, a transition will be expected for $\gamma = 1$.

It is convenient to define a degree of coverage, according to the relation of the area covered by the circle (or the stripes) to the area of the square surface in which it is inscribed:

$$\theta = \frac{S}{d^2}. \tag{8}$$

The transition at $\gamma = 1$, implies from equation (7) that $d = \pi^{1/2} S_{\mathrm{crit}}^{1/2}$ and the critical coverage becomes:

$$\theta_{\mathrm{crit}} = \frac{S_{\mathrm{crit}}}{d_{\mathrm{crit}}^2} = \frac{1}{\pi}. \tag{9}$$

In other words, for $\theta < \frac{1}{\pi} \approx 0.32$ the circular phase is more stable, while for $\theta > \frac{1}{\pi} \approx 0.32$ the striped phase is more stable.

In the present nanocavity problem, the positive curvature inside the nanostructure makes the initial growth take an approximately circular shape inside it, with a more or less ordered pattern on the surface. As the degree of coverage increases, circular growth proceeds until a point where stripes growing across the system are more stable, and growth proceeds this way. It would be interesting to see if the transition from circular growth to stripes takes places at a coverage close to that predicted by the present simplified model. In our case, for a nanodot 40 nm in size the d value will be larger than 60 nm to have $\theta < \frac{1}{\pi} \approx 0.32$. As the typical nanocavity–nanocavity distance is slightly smaller (50 nm) the transition to ripples takes place as soon the dots reach the nanocavity dimension.

The present model could also be formulated taking into account the 3D structure of the deposits. For example, if instead of a 'circle–band' transition, a 'hemisphere–half cylinder' transition is considered, the energy criterion will be the interfacial tension. In this case, it is useful to redefine the γ factor from above according to:

$$\gamma = \frac{V/(2\pi R^2)}{V/(\pi r l)} \tag{10}$$

where $V/(2\pi R^2)$ is now the volume to area ratio of a hemisphere of radius R, and $V/(\pi r l)$ is the volume to area ratio of a half cylinder of length l and radius r. Thus, the transition is expected to take place when $rl/2R^2 = 1$. To get a relationship between r and R we assume mass conservation, so that we can equate the volume of the hemisphere V_{hs} and the volume of the half cylinder V_{hc} according to:

$$V_{\mathrm{hs}} = \frac{2}{3}\pi R^3 = V_{\mathrm{hc}} = \frac{\pi r^2 l}{2}. \tag{11}$$

From the latter equation we obtain $r = (\frac{4R^3}{3l})^{1/2}$ so the transition is expected to take place when $R = l/3$. As before, we can define a degree of coverage for the hemispheres, according to the equation:

$$\theta_{\mathrm{hs}} = \frac{\pi R^2}{l^2} \tag{12}$$

so that the critical coverage for the hemispheres is expected to be $\theta_{\mathrm{hs,crit}} = \frac{\pi}{3} \approx 0.35$, very close to the value we obtained above for the 2D model.

Finally, a comment should be made about the preferential deposition at the nanocavities. The argument concerning preferential deposition in concavities (equation (1)) is a thermodynamic one and also has a chemical basis: sites with a higher coordination should provide more stable adsorption sites. Thus, on energetic grounds metal deposition should be preferred there, giving place to a nucleation process. Once planarity is reached, the atoms of the growing phase may: (a) deposit on the growing phase, forcing convexity, (b) deposit on and adjacent to the growing phase, further covering the surface in a planar fashion. If charge transfer is faster on the growing phase than on the upd adlayer, Ag atoms will deposit on the cavities. The high activation energy involved with the motion of Ag adatoms over a descending step may be responsible for the forced convexity observed. This explanation is similar to that proposed in [23] to explain the wetting–nonwetting transition. In short, steps (I)–(III) in figure 10 appear to be determined by the thermodynamics of the system and step (IV) by the kinetics.

Note that our model is based only on geometric considerations and the chemistry does not play any role in the dot to ripple transition. We have observed the dot to ripple transition for Cu nanodots grown on patterned Au and also for copper sulfide nanodots formed on patterned Cu. However, further experimental work is necessary to confirm the validity of the proposed model.

4. Conclusions and outlooks

Silver nanodots and nanoripples can be grown on nanocavity-patterned Au templates by tuning the electrodeposition potential and charge density. For potential values close to the reversible potential for Ag electrodeposition Ag monolayers can be preferentially deposited at nanocavities. The Ag-coated nanocavities act as preferred sites for instantaneous nucleation and growth of the 3D metallic dots ∼40 nm in lateral size and ∼4 nm in average height with a spatial distribution dictated by the template. A simple model based on minimization of surface free energy indicates that dots are in a metastable state so that further Ag deposition drives the system to nanostripe formation. The cavity–cavity distance and the dot size along the deposition process should be crucial to determine the final structure of the system. In our next paper we will use the Ag-coated cavities to prepare a high density of silver sulfide and silver oxide nanostructures on polymer-supported metal templates.

Acknowledgments

We acknowledge financial support from ANPCyT (PICT02-11111 and PICT02-12485), CONICET (PIP 6075) and Fundación Antorchas. PLS also thanks CONICET for financial support for this work. This paper was made in the frame of the Interfacial, Supramolecular and Molecular Nanoscience and Nanotechnology Net (Argentina).

References

[1] Timp G 1999 *Nanotechnology* (New York: Springer)
[2] Lian J, Zhou W, Wang L, Boatner L A and Ewing R C 2005 *Microsc. Microanal.* **11** (Suppl. 2) 87
[3] Rusponi S, Constantini G, Boragno C and Valbusa U 1998 *Phys. Rev. Lett.* **81** 2735
[4] Erlebacher J D, Chason E H, Sinclair M B, Floro J A and Aziz M J 1999 *Phys. Rev. Lett.* **82** 2330
[5] Mayer T M, Chason E and Howard A J 1994 *J. Appl. Phys.* **76** 1633
[6] Vattuone L, Burghaus U, Savio L, Rocca M, Constantini G, Bautier de Mongeot F, Boragno C, Rusponi S and Valbusa U 2001 *J. Chem. Phys.* **115** 3346
[7] Facsko S, Dekorsky T, Koerdt C, Trappe C, Kurz H, Vogt A and Hartnagel H L 1999 *Science* **285** 1551
[8] Zwiller V, Aichele T and Benson O 2004 *New J. Phys.* **6** 96
[9] Jin G, Liu J L, Thomas S G, Luo Y H, Wang K L and Nguyen B-Y 1999 *Appl. Phys. Lett.* **75** 2752
[10] http://pr.fujitsu.com/en/news/2002/07/29.html
[11] Schlesinger M and Paunovic M (ed) 2000 *Modern Electroplating* 4th edn (New York: Wiley)
[12] Engelmann G E, Ziegler J C and Kolb D M 1998 *Surf. Sci.* **401** L420
[13] Schilardi P L, Dip P, dos Santos Claro P C, Benitez G A, Fonticelli M H, Azzaroni O and Salvarezza R C 2006 *Chem. Eur. J.* **12** 38
[14] Hernández Creus A, Gimeno Y, Salvarezza R C and Arvia A J 2004 *Encyclopedia of Nanoscience and Nanotechnology* vol 2, ed H S Nalwa (North Lewis Way, CA, USA: American Scientific Publishers) pp 221–35
[15] Walters R, Biteen J, Atwater H and Bourianoff G 2004 *Laser Focus World* September
[16] Lu Y, Liu G L and Lee L P 2005 *Nano Lett.* **5** 5
[17] Zoval J V, Stiger R M, Biernacki P R and Penner R M 1996 *J. Phys. Chem.* **100** 837
Stiger R M, Craft B, Gorer S A and Penner R M 1999 *Langmuir* **15** 790
[18] Gago R, Vázquez L, Cuerno R, Varela M, Ballesteros C and Albella J M 2001 *Appl. Phys. Lett.* **78** 3316
[19] Azzaroni O, Fonticelli M, Benítez G, Schilardi P L, Gago R, Caretti I, Vázquez L and Salvarezza R C 2004 *Adv. Mater.* **16** 405
[20] Lee J, Oh I, Hwang S and Kwak J 2002 *Langmuir* **18** 8025
Esplandiu M J, Schneeweiss M A and Kolb D M 1999 *Phys. Chem. Chem. Phys.* **1** 4847
Ogaki K and Itaya K 1995 *Electrochim. Acta* **40** 1249
Chen C H, Vesecky S M and Gerwirth A A 1992 *J. Am. Chem. Soc.* **114** 451
[21] Carro P, Ambrosolio S, Marchiano S L, Hernández Creus A, Salvarezza R C and Arvia A J 1995 *J. Electroanal. Chem.* **396** 183
Schilardi P L, Marchiano S L, Salvarezza R C, Hernández Creus A and Arvia A J 1997 *J. Electroanal. Chem.* **431** 81
[22] Corcoran S G, Chakarova G S and Sieradzki K 1994 *J. Electroanal. Chem.* **377** 85
[23] Corcoran S G, Chakarova G S and Sieradzki K 1993 *Phys. Rev. Lett.* **71** 1585
[24] Luque N B, Del Pópolo M G and Leiva E P M 2004 *Surf. Sci.* **571** L319
[25] Luque N B and Leiva E P M *56th Annual Meeting of the International Society of Electrochemistry (Busan, Korea, Sept. 2005)* p 984 (Abstract Number 7-010-O)
[26] Pimpinelli A and Villain J 1998 *Physics of Crystal Growth* (Cambridge: Cambridge University Press)